

## Evaluation of the elasticity normal to the basal plane of non-expandable 2:1 phyllosilicate minerals by nanoindentation

GUOPING ZHANG,<sup>1,\*</sup> ZHONGXIN WEI,<sup>1</sup> RAY E. FERRELL,<sup>2</sup> STEPHEN GUGGENHEIM,<sup>3</sup>  
RANDALL T. CYGAN,<sup>4</sup> AND JIAN LUO<sup>5</sup>

<sup>1</sup>Department of Civil and Environmental Engineering, Louisiana State University, Baton Rouge, Louisiana 70803, U.S.A.

<sup>2</sup>Department of Geology and Geophysics, Louisiana State University, Baton Rouge, Louisiana 70803, U.S.A.

<sup>3</sup>Department of Earth and Environmental Sciences, University of Illinois at Chicago, Chicago, Illinois 60607, U.S.A.

<sup>4</sup>Geochemistry Department, Sandia National Laboratories, Albuquerque, New Mexico 87185, U.S.A.

<sup>5</sup>School of Materials Science and Engineering, Clemson University, Clemson, South Carolina 29634, U.S.A.

### ABSTRACT

Nanoindentation experiments were conducted to investigate the elasticity normal to the basal plane of six non-expandable, hydrous 2:1 phyllosilicate minerals (pyrophyllite, talc, biotite, two muscovite samples, and margarite) with layer charge  $z$  ranging from 0 to 1.823 per  $\text{O}_{10}(\text{OH})_2$ . For the examined indentation depth  $h$  of  $\leq 200$  nm, the measured Young's modulus  $E$  decreases with increasing  $h$ . Furthermore, the rate of reduction in the apparent  $E$ , in general, decreases with increasing  $z$ . The dependence of apparent  $E$  on  $h$  is attributed to indentation-induced inelastic deformation, particularly the deformation related to the high local stresses beneath the indenter tip, such as kink band formation, layer delamination, void generation, and cracking, which tend to cause damage to the layer structure. To minimize the influence of inelastic deformation on the measurement of  $E$  by indentation, the maximum  $E$  at small  $h$  is proposed to be the truly representative elastic modulus. The stiffest species, margarite, with  $z = 1.823$ , has a representative  $E$  of 165.5 GPa, seven times greater than that of pyrophyllite with  $z = 0$  and  $E = 23.5$  GPa. A nearly linear correlation between the representative  $E$  and the square of the ratio of the surface charge density  $\sigma$  to half of the basal spacing  $d(001)$ ,  $[2\sigma/d(001)]^2$ , exists. This relationship suggests that the elasticity normal to the basal plane of these phyllosilicates is primarily controlled by the long-range electrostatic attractions between the 2:1 layer and interlayer cations instead of atomic bonds within the 2:1 layer, although other compositional and structural variations also affect the interlayer interactions. This relationship may indicate that the interlayer complexes can be used as the elasticity signatures of phyllosilicate minerals.

**Keywords:** Elasticity, interlayer interactions, nanoindentation, phyllosilicates, Young's modulus

### INTRODUCTION

Hydrous phyllosilicate minerals are ubiquitous in the geosphere, and their elastic behavior significantly affects the stiffness, compression, and stored elastic energy of the Earth's crust. Common phyllosilicates, such as clay minerals, significantly affect the overall elastic behavior and propagation of seismic waves in crustal environments (e.g., Vernik and Liu 1997; Wang et al. 2001). The remote imaging and probing of Earth properties at increased resolution and accuracy using seismic waves require the knowledge of the elastic properties of all solid constituents in a geological stratum. Therefore, understanding the elasticity of phyllosilicate minerals has direct and significant importance for probing the geophysical signatures of minerals and rocks and for geophysical sensing of the compositions of the Earth's subsurface and of the processes therein.

Phyllosilicate minerals are platy in shape, possess complex layer crystal structures, and are characterized by variable permanent layer charges, a variety of interlayer complexes, and distinctive basal spacings,  $d(001)$ . These minerals consist of either discrete or mixed-layer sequences of fundamental 1:1 lay-

ers of 0.7 nm in thickness or 2:1 layers of 1.0 nm in thickness, with sub-nanometer interlayers, and hence they are naturally occurring nanostructured multilayer materials. These structural and compositional variations are expected to affect elasticity and related properties, such as seismic wave velocities and deformations. The elasticity of conventional continua, including most other aluminosilicate minerals, is controlled by atomic bonding (e.g., ionic, covalent, or metallic bonds) (e.g., Eberhart 1996) where elastic deformation is typically caused by reversible bond stretching, and inelastic deformation usually involves bond rearrangements or breakage (e.g., Baker et al. 2002). For phyllosilicate minerals, however, interlayer interactions, such as van der Waals forces, interlayer cation hydration, Born repulsion, and electrostatic forces between positively charged interlayer cations and negatively charged 2:1 or 1:1 layers, are generally much weaker than the atomic bonds within the 1:1 or 2:1 layer. As such, these interlayer interactions may play vital roles in controlling the elasticity of phyllosilicates, particularly in the direction normal to the basal plane. However, accurate, quantitative correlations between the interlayer interactions and elasticity have yet to be determined. Therefore, understanding the elasticity of these complex minerals is a fundamental query

\* E-mail: gzhang@lsu.edu

of the physics of elasticity, and such knowledge may extend conventional elasticity theory to more complex nanostructured phyllosilicate minerals or other nanostructured multilayer composites in natural and synthetic materials.

Experimentally, the elastic properties of phyllosilicate minerals are usually studied by Brillouin spectroscopy (e.g., Vaughan and Guggenheim 1986; McNeil and Grimsditch 1993; Wang et al. 2006) and X-ray or neutron diffraction using a diamond anvil cell or tungsten carbide anvil cell (e.g., Hazen and Finger 1978; Pawley et al. 1995; Dera et al. 2003; Zanazzi et al. 2007). The present study utilizes a nanomechanical testing technique, nanoindentation, to investigate the elasticity of some non-expandable hydrous phyllosilicate minerals. This analysis is restricted to the direction normal to the basal plane or [001]\* for two reasons: (1) the difficulty in making indentation in directions parallel to the basal plane, and (2) the significant variability and complexity in [001]\* elasticity. A special feature of nanoindentation is that plastic or inelastic deformation is usually generated by indentation loading and hence may provide additional insight into the significance of interlayer interactions. In addition, nanoindentation, a relatively simple, non-destructive technique, can be performed on limited sample material or on very small crystals (Fischer-Cripps 2002), such as clay minerals.

## EXPERIMENTAL METHODS

Six well-analyzed macrocrystalline 2:1 phyllosilicate minerals, pyrophyllite, talc, biotite, two muscovite samples, and margarite (Table 1), with known geographical origin, structure, and chemical composition (Guggenheim and Bailey 1975; Lee and Guggenheim 1981; Guggenheim et al. 1987; Rancourt et al. 1992; Russell and Guggenheim 1999) were chosen, because they represent two octahedral compositional series of non-expandable 2:1 type minerals. Talc generally does not vary in composition and this sample is expected to be similar to that described by Perdikatsis and Burzlaff (1981). This talc sample also shows excellent crystallinity as determined by single-crystal X-ray analysis. Talc and pyrophyllite have no interlayer cations, and the uncharged 2:1 layers are bonded principally by van der Waals forces. The other four samples, margarite, biotite, and two muscovites, in contrast, have net negatively charged 2:1 layers and contain non-hydrated or unsolvated interlayer cations. Their layers are bonded by primarily electrostatic forces. The layer charges ( $z$ ) of these samples ranging from 0 to 1.823 per  $O_{10}(\text{OH})_2$  (Table 2) result almost entirely from isomorphous substitutions of Al for Si in the tetrahedra, which simplifies interpretation of the experimental results. The locus of layer charge (i.e., tetrahedra vs. octahedra) may complicate the electrostatic interactions between the layer and interlayer cations. If isomorphous substitutions occur in tetrahedra, there is relatively concentrated electrostatic charge near the basal oxygen triad of the substituted tetrahedra of the siloxane surface adjacent to the interlayer. In contrast, any octahedral substitutions produce a relatively diffuse electrostatic charge at the basal plane adjacent to the interlayer. Pyrophyllite, muscovite, and margarite are dioctahedral phyllosilicates having two Al cations and a vacancy for every three sites in the octahedral sheet, whereas trioctahedral talc and biotite have three fully occupied octahedral sites, typically containing divalent cations, such as Mg or Fe.

Carefully selected cleavage fragments of the six samples with an in-plane dimension of >1.0 mm and a thickness of >100  $\mu\text{m}$  were glued onto a single-crystal silicon wafer (100) (MTI Corporation, Richmond, California) substrate using melted Crystalbond 509 amber resin (Aremco Products, Inc., New York)

heated to 130 °C. Overheating of the sample was avoided by removing the heated silicon wafer substrate immediately after sample placement, and the mineral basal plane was mounted as parallel to the wafer surface as possible. A very thin layer was cleaved off the surface of each sample so that a fresh and intact surface is exposed to accept indentation.

Nanoindentation tests were performed using an MTS Nano XP indenter (MTS Nano Instruments, Inc., Oak Ridge, Tennessee) at ambient conditions. A dynamic contact module (DCM) head equipped with a Berkovich tip with a tip radius of <20 nm was used to indent the samples under a continuous stiffness measurement (CSM) mode at a constant indentation strain rate ( $\dot{h}/h$ ) of 0.05  $\text{s}^{-1}$ , where  $h$  is indentation depth. The DCM head has a load resolution of 1.0 nN and displacement resolution of <0.01 nm. The CSM mode involved the superimposing of a displacement-controlled harmonic loading with a frequency of 75 Hz and an amplitude of 1.0 nm. All tests were run with an allowed thermal drift rate of <0.03 nm/s and used the five-step loading procedure depicted in Figure 1: (1) increase load at a constant indentation strain rate of 0.05  $\text{s}^{-1}$  to a pre-selected maximum indentation depth ( $h_{\text{max}}$ ) of about 200 nm; (2) hold maximum load  $F_{\text{max}}$  constant for a given hold time  $t_h = 10$  s, where  $F$  is indentation load; (3) decrease  $F$  under load control mode using the same loading rate ( $dF/dt$ ) as that at  $F_{\text{max}}$  of loading part to 10% of  $F_{\text{max}}$ ; (4) hold the load (at 10% of  $F_{\text{max}}$ ) constant for 100 s to record the thermal drift of the instrument; and (5) decrease  $F$  linearly to zero.

For each sample, a rigorous four-step testing scheme was employed to ensure high reliability and accuracy of the results: (1) tip cleaning by indenting (nine indents) on a piece of Scotch double-sided sticky tape; (2) pre-testing of tip by indenting on standard fused silica to calibrate the tip and check the instrument working status; (3) making multiple indents (typically 4–9 indents as an array of  $2 \times 2$ ,  $3 \times 3$ , or  $2 \times 3$ , depending on the size of an available clean and intact area on the mineral surface) with a spacing of 100  $\mu\text{m}$  on a smooth region of the sample surface selected under the optical microscope installed with the nanoindenter; and (4) post-testing tip checking by indenting on the same standard fused silica. If the hardness and elastic modulus of the fused silica measured in Steps 2 and 4 deviated from the standard values significantly, the results obtained in Step 3 were discarded and a new measurement was performed again starting from Step 1.

The Young's modulus was derived from the load  $F$ , indentation depth  $h$ , and harmonic contact stiffness  $S$  recorded during the loading section of the test by using the Oliver and Pharr method (Oliver and Pharr 1992, 2004; Li and Bhushan 2002). An elastic parameter, reduced modulus ( $E_r$ ), is obtained from

$$E_r = \frac{\sqrt{\pi}}{2\beta\sqrt{A_c}} S \quad (1)$$

where  $\beta$  is a dimensionless correction factor for the indenter tip shape, and  $\beta = 1.05$  is commonly recommended for a Berkovich indenter (Oliver and Pharr 2004);  $A_c$  is the projected contact area between the indenter and sample, which is obtained through the contact depth  $h_c$  (Oliver and Pharr 1992)

$$A_c = C_0 h_c^2 + \sum_{j=1}^8 C_j h_c^{\left(\frac{j}{2}\right)^{-1}} \quad (2)$$

where  $h_c$  can be determined by

$$h_c = h - \frac{F}{\epsilon S} \quad (3)$$

where  $\epsilon$  is a constant that depends on indenter tip geometry (for a Berkovich tip,  $\epsilon = 0.75$ ). For a perfect Berkovich indenter, the leading term  $C_0$  is 24.5;  $C_j$  ( $j = 1, 2, \dots, 8$ ) are needed to describe the deviations of the tip shape from the perfect Berkovich geometry owing to tip blunting. These constants were determined

**TABLE 1.** Name, origin, and chemical formula of the six mineral samples

Name	Origin	Octahedral type	Formula
Margarite-2M <sub>1</sub>	Chester County, Pennsylvania	Di	(Ca <sub>0.81</sub> K <sub>0.01</sub> Na <sub>0.19</sub> )(Al <sub>1.99</sub> Fe <sub>0.01</sub> Mg <sub>0.03</sub> )(Si <sub>2.11</sub> Al <sub>1.89</sub> )O <sub>10</sub> (OH) <sub>2</sub>
Muscovite-2M <sub>1</sub> (P)	Panasqueira, Portugal	Di	(K <sub>1.00</sub> Na <sub>0.03</sub> Ca <sub>0.01</sub> )(Al <sub>1.93</sub> Fe <sub>0.07</sub> Mg <sub>0.01</sub> Mn <sub>0.01</sub> )(Si <sub>3.08</sub> Al <sub>0.91</sub> )O <sub>10</sub> (OH) <sub>1.88</sub> F <sub>0.12</sub>
Muscovite-2M <sub>1</sub> (SD)	Diamond Mine, Keystone, South Dakota	Di	(K <sub>0.93</sub> Na <sub>0.08</sub> Ca <sub>0.01</sub> )(Al <sub>1.83</sub> Fe <sub>0.16</sub> Mn <sub>0.01</sub> )(Si <sub>3.10</sub> Al <sub>0.90</sub> )O <sub>10</sub> (OH) <sub>1.83</sub> F <sub>0.17</sub>
Biotite-1M	Silver Crater Mine, Bancroft, Ontario	Tri	(K <sub>0.93</sub> Na <sub>0.08</sub> )(Mg <sub>1.57</sub> Fe <sub>1.17</sub> Ti <sub>0.11</sub> Mn <sub>0.06</sub> )(Si <sub>2.97</sub> Al <sub>1.00</sub> Ti <sub>0.03</sub> )O <sub>10</sub> (OH) <sub>1.05</sub> F <sub>0.94</sub> Cl <sub>0.01</sub> )
Talc-1T <sub>c</sub>	Mont Windara, Australia	Tri	(Mg <sub>3</sub> )(Si <sub>4</sub> )O <sub>10</sub> (OH) <sub>2</sub> *
Pyrophyllite-1T <sub>c</sub>	Ibitiara, Bahia, Brazil	Di	(Al <sub>1.97</sub> Fe <sub>0.03</sub> )(Si <sub>3.98</sub> Al <sub>0.02</sub> )O <sub>10</sub> (OH) <sub>2</sub>

\* Ideal formula.

**TABLE 2.** Summary of crystallographic data, representative Young’s modulus, and surface charge density of the six samples

Name	$E_{rep}$ (GPa)	$z$	$a$ (nm)	$b$ (nm)	$d(001)$ (nm)†	$\sigma$ (C/m <sup>2</sup> )
Margarite	165.5 ± 0.2	1.823	0.5104	0.8829	0.9468	0.65
Muscovite (P)	83.5 ± 5.4	1.05	0.5158	0.8951	0.9985	0.36
Muscovite (SD)	77.4 ± 4.2	1.03	0.5200	0.9021	0.9979	0.35
Biotite	37.1 ± 0.9	1.01	0.5335	0.9242	1.0016	0.33
Talc*	28.7 ± 4.3	0	0.5290	0.9173	0.9351	0.00
Pyrophyllite	23.5 ± 1.1	0.02	0.5160	0.8966	0.9144	0.01

\* Data derived from Perdikatsis and Burzlaff (1981), but not specifically from the sample used.  
 †  $d(002)$  for two-layer polytypes.

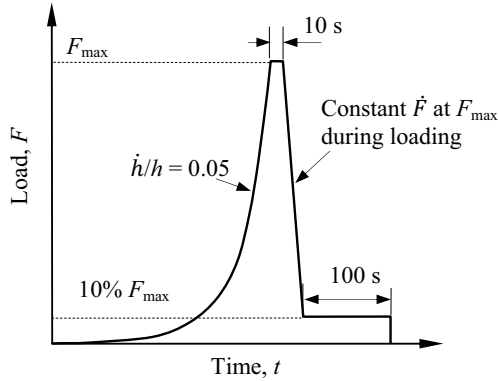


**FIGURE 1.** The DCM loading and unloading profile used in all nanoindentation tests.

through tip calibration indentation tests on standard fused silica with a Young’s modulus  $E$  of 72 GPa.

The elastic modulus of the sample is extracted by (Johnson 1985; Doerner and Nix 1986)

$$\frac{1}{E_r} = \frac{1 - \nu^2}{E} + \frac{1 - \nu_i^2}{E_i} \quad (4)$$

where  $\nu$  and  $\nu_i$  are the Poisson’s ratios of the sample and indenter, and  $E$  and  $E_i$  are the Young’s modulus of the sample and indenter, respectively. For a diamond indenter,  $E_i = 1141$  GPa, and  $\nu_i = 0.07$ . Because previous studies suggest that the Poisson’s ratio of the tested material has no significant influence on the Young’s modulus (e.g., Mencik et al. 1997), a constant  $\nu = 0.25$  is assumed for all six samples (Mavko et al. 1998). Because the loading direction is normal to the basal plane, the derived elastic modulus  $E$  is referenced to the [001]\* direction.

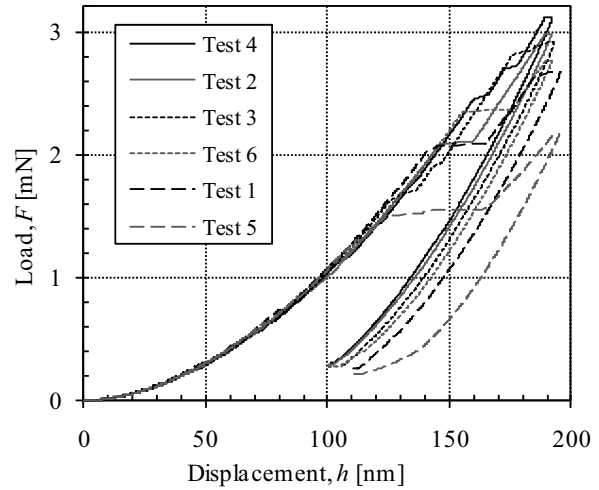
**RESULTS AND DISCUSSION**

**Indentation load-displacement curves**

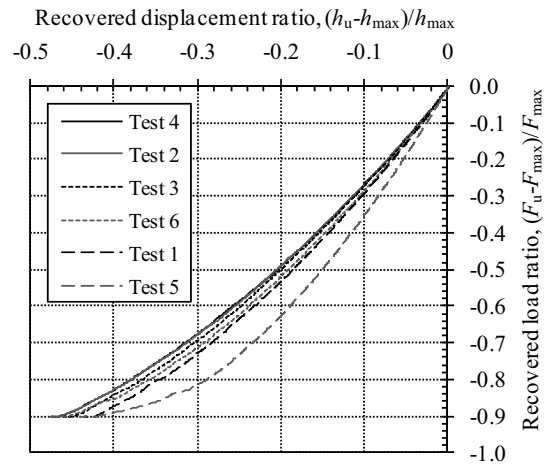
The six phyllosilicate samples exhibit similar indentation load-displacement curves. We present only the typical curves obtained from muscovite (SD) at six different locations. Figure 2a shows each entire curve with unloading, whereas Figure 2b compares only the unloading sections of the six curves. In Figure 2a, a striking feature is the presence of multiple, randomly occurring giant discontinuities (also called displacement bursts) or pop-ins of varying magnitudes or extensions (e.g., the maximum pop-in is ~50 nm, accounting for nearly 25% of the maximum indentation depth of ~200 nm) in the loading portion of the curves. Before the occurrence of the giant pop-ins around  $h = \sim 120$  nm, the loading sections of each curve are consistent, although careful examination also found that small pop-ins with an extension of ~1.0 nm occur as early as at depths of 11–16 nm. In general, the greater

the pop-in extension, the smaller the maximum load required to reach a given displacement (these tests were conducted under displacement control mode) and the greater the reduction in the slope of the section of the loading curve following a giant pop-in. A reduction in the slope of the loading curve reflects a decrease in the resistance of the sample to penetration. As discussed below, a giant pop-in causes damage to the sample in the region influenced by the indenter-induced stresses.

The occurrence of indentation pop-ins in materials with layered structure (e.g., muscovite, graphite, MoS<sub>2</sub>, Ti<sub>3</sub>SiC<sub>2</sub>) has been attributed to several deformation mechanisms, such as kink band formation and associated layer delamination and void introduction, and cracking (including both radial and lateral cracks). Owing to the inherent layer structure, dislocation glide planes are confined parallel to the basal plane, and continuous generation of dislocations results in the formation of kind bands,



(a)



(b)

**FIGURE 2.** Indentation load-displacement curves for muscovite (SD) obtained at six different indent locations: (a) entire curves showing loading and unloading, and (b) the unloading portion of the curves.

which are always accompanied by layer delamination and void introduction (e.g., Molina-Aldareguia et al. 2003; Barsoum et al. 2004a, 2004b; Schuh 2006; Zhang et al. 2009a). Further stressing or deformation causes the fracture or rupture of the basal planes along a kink band boundary. In addition, excessive penetration of the indenter into muscovite promotes the formation of both radial cracks emanating from the sharp edges of the indenter and lateral cracks confined between the radial cracks (Zhang et al. 2009a). Such damage through cracking and layer delamination influences the penetration resistance of the phyllosilicate minerals.

The change in the properties of the sample with indentation depth owing to indentation-induced damage is also demonstrated by the comparison of the unloading curves shown in Figure 2b. In this figure,  $F_u$  and  $h_u$  are the indentation load and displacement recorded during unloading, respectively. Each test was unloaded to 10% of  $F_{max}$ . However, the recovered displacement varies among these tests, although indentation unloading is typically regarded as involving elastic deformation only. The giant pop-ins that occur in the loading segment apparently affect the unloading behavior. The larger the extension of a pop-in, the smaller the percent of recovered displacement. The unloading curve of Test 5 with an “elbow” shape is similar to that observed by Oliver et al. (2007, 2008) on silicon and germanium, two highly brittle semiconducting materials. In their work, giant pop-ins observed during indentation loading were attributed to spallation and/or associated material removal triggered by lateral cracking. The unusual elbow-shaped unloading curves are a result of the elastic recovery of some of the delaminated (because of lateral cracking), but not fully detached lateral chips acting as cantilevers. Zhang et al. (2009b) also reported a similar phenomenon observed during indentation of a Grade V-4 muscovite sample (SPI supplies, West Chester, Pennsylvania). Figure 3 demonstrates the occurrence of extensive radial and lateral cracks caused by indentation on the muscovite. If the elastic unloading behavior is affected by the giant pop-ins, then the Young’s modulus  $E$  measured through CSM method during loading should also be influenced by the giant pop-ins, as is demonstrated by the derived Young’s modulus described below.

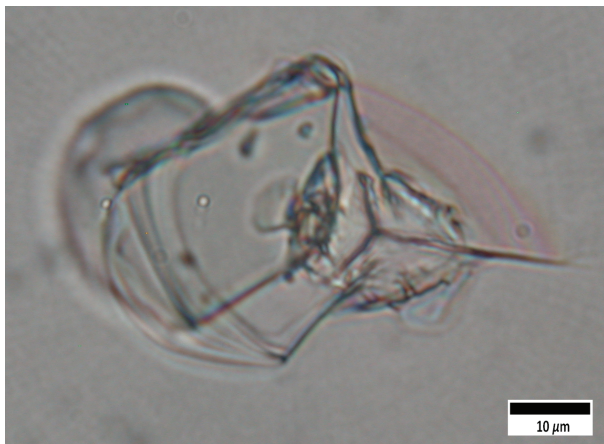


FIGURE 3. An optical micrograph of a residual indent in a muscovite showing the occurrence of radial cracks, lateral cracks, and chip removal.

To compare the indentation load-displacement curves of each sample, a single curve statistically averaged over multiple indentations was obtained. Figure 4 illustrates the loading portion of the averaged load-displacement curves of all samples, where randomly occurring pop-ins are not observable after averaging. Different samples exhibit variable resistance to indentation penetration, which usually includes both elastic and inelastic or plastic deformations. In general, the higher the layer charge  $z$ , the stronger the penetration resistance. The load required to reach a given  $h$  increases from pyrophyllite and talc ( $z \approx 0$ ), to biotite and muscovite ( $z \approx 1.0$ ), and to margarite ( $z = 1.823$ ). The penetration resistance is presumably related to the interlayer cohesiveness. Pyrophyllite and talc have the lowest resistance, because primarily van der Waals attractive forces exist between their layers. Interlayer forces for the other four samples include relatively strong electrostatic attractions between the 2:1 layer and interlayer cations resulting in increased resistance. Again, owing to their layer structure that restricts the dislocation movement, kink band formation is the major source of plastic deformation, which is always accompanied by layer delamination. Therefore, interlayer cohesiveness controls the indentation loading behavior. Moreover, different indentation responses between the two muscovite samples and between talc and pyrophyllite are remarkably discerned by nanoindentation. As discussed below, this difference is caused by the structural and/or layer charge variations that affect the interlayer cohesiveness.

#### DERIVED ELASTIC MODULUS

Figure 5a plots the derived Young’s modulus  $E$  against  $h$ . In general, except for the initial small portion of the curves at a few nanometers displacement, the measured  $E$  decreases with increasing  $h$ , indicating that the apparent  $E$  values are dependent upon indentation depth. One or more of the following deformation mechanisms probably contribute to the dependence of  $E$  on  $h$ : (1) kink band formation in layer silicates and associated layer delamination and void formation, the latter two being inherent to kink bands (e.g., Barsoum et al. 2004a, 2004b); (2) formation of radial cracks emanating from the corners of indents and lateral

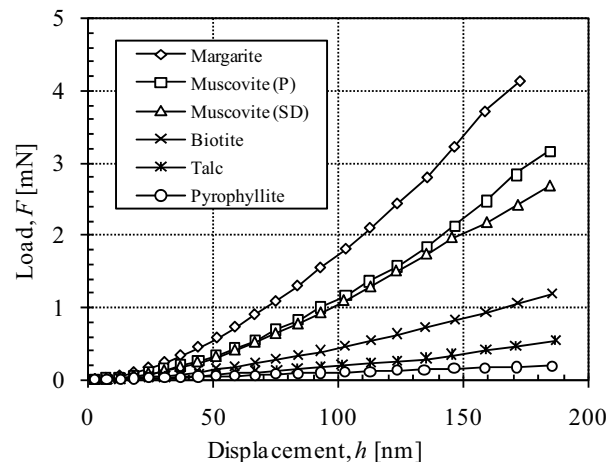
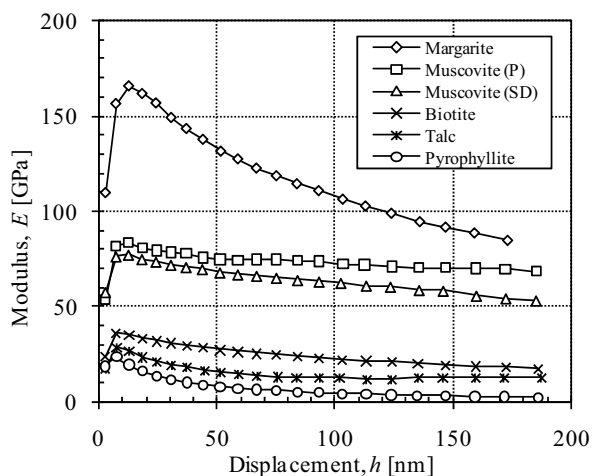
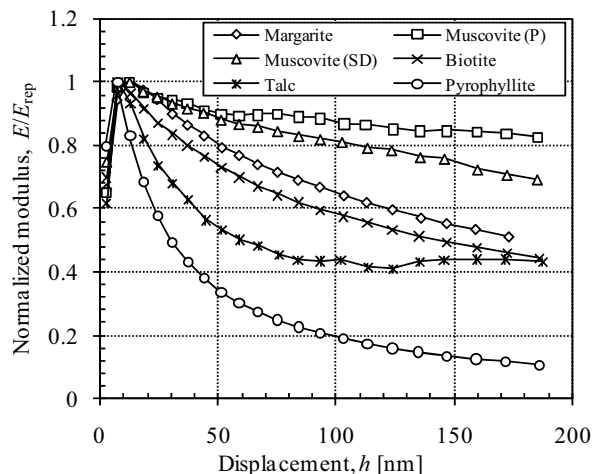


FIGURE 4. Average indentation load-displacement curves for the six samples.



(a)



(b)

FIGURE 5. The measured Young's modulus of the six samples: (a) the relationship between  $E$  and  $h$ ; (b) the relationship between  $E/E_{\text{rep}}$  and  $h$ .

cracks (for layered materials with relatively weak interlayer cohesiveness, lateral crack and layer delamination are indistinguishable and these two deformation modes are essentially the same), as observed in the Grade V-4 muscovite (Fig. 3); and (3) nonlinear elasticity caused by the formation and annihilation of incipient kink bands in layer minerals such as graphite and muscovite (Barsoum et al. 2004a, 2004b). A more definitive investigation of the mechanisms underlying this observed phenomenon is ongoing.

Because the measured  $E$  decreases with  $h$ , the maximum  $E$  value obtained at small  $h$ , and hence load  $F$ , probably represents the true elastic modulus ( $E_{\text{rep}} = E_{\text{max}}$ ). This interpretation avoids the influence of indentation-induced inelastic deformation discussed above on the determination of  $E$ . The results are summarized in Table 2. The  $E_{\text{rep}}$  increases significantly with layer charge  $z$  and spans a wide range, 23.5 GPa for pyrophyllite ( $z$

= 0) to 165.5 GPa ( $z = 1.823$ ) for margarite, about seven times greater. Small variations in  $E_{\text{rep}}$  values resulting from structural and compositional variations (e.g., the two muscovite samples and the dioctahedral vs. trioctahedral phases) were also probed by high-resolution nanoindentation testing. Prior studies concluded that a single 2:1 layer excluding interlayer complexes has a Young's modulus of ~250–260 GPa (e.g., Manevitch and Rutledge 2004; Chen and Evans 2006; Podsiadlo et al. 2007), which is an order of magnitude greater than the  $E_{\text{rep}}$  of talc and pyrophyllite and 1.6 times greater than the maximum  $E_{\text{rep}}$  of margarite. Thus, the  $E$  reduction between a single 2:1 layer and a multilayer 2:1 crystal is mainly a function of interlayer cohesiveness. Different interlayer compositions and topologies result in different degrees of  $E$  reduction, with talc and pyrophyllite (no interlayer cations) undergoing the largest reduction and margarite (highest  $z$ ) the smallest.

For phyllosilicate minerals, changes in bonding that occur in the interlayer must affect the octahedral and tetrahedral sheets and vice versa (e.g., Bailey 1984). For example, the interlayer cation in the micas has been shown to affect the position of the O-H vector at the octahedral and tetrahedral sheet common junction. Also, the position of the O-H vector differs between dioctahedral and trioctahedral phases. In trioctahedral structures, the O-H vector points toward the interlayer cation at ~60 to ~90° from the (001) depending on the charge (1+ or 2+) of the occupant in  $M1$  (in the case of divalent Mg where all three octahedral sites are occupied by Mg, the angle is near 90°); as such, the O-H vector reduces the strength of the bonding between the cation and 2:1 layer. In dioctahedral phyllosilicates, the O-H vector is close to the (001) at roughly 0° from the basal plane, and does not weaken the bonding between the interlayer cation and 2:1 layer as much. In contrast, where there is no interlayer cation (talc and pyrophyllite), the O-H vector does not play this role of weakening the bonding between the layers. Therefore, although the trioctahedral biotite sample has nearly the same  $z$  as the two dioctahedral muscovite samples, its  $E$  values are much smaller, owing to the weakening of the electrostatic interactions between the interlayer cation and 2:1 layer by the O-H vector.

Additional information can be obtained by considering the rate of change in  $E$  over  $h$ . Figure 5b plots the  $E$  normalized by the  $E_{\text{rep}}$  of each sample against  $h$ . Clearly, the rate of  $E$  reduction decreases with increasing  $z$ , with the exception of margarite ( $z = 1.823$ ). The two muscovite samples have the smallest rate of reduction, whereas the pyrophyllite shows the highest rate. This difference may also originate from different modes of inelastic deformation, such as kink band formation, layer delamination, and cracking, and the dominance of one type over the others. The weaker interlayer bonding (i.e., van der Waals forces only) in pyrophyllite and talc may result in easy layer delamination, resulting in a fast reduction of  $E$  over  $h$ . The stronger interlayer bonding (i.e., primarily electrostatic attraction forces) in the two muscovite samples may delay the formation of layer delamination and associated kink band formation and cracking, resulting in a slower rate of reduction of  $E$  over  $h$ . For margarite, the interlayer bonding may be so strong that it behaves much more brittle than muscovite, and hence cracking may easily occur and propagate, resulting in a faster rate of decrease in  $E$  over  $h$ . Unfortunately, owing to the very small residual indents caused

by a small indenter tip under small indentation load, searching for or imaging the residual indents was not successful. The lack of detectable residual indents may also be partly a result of non-linear, reversible elastic deformation associated with incipient kind bands, which leaves no residual imprints (Barsoum et al. 2004a, 2004b). Nevertheless, further investigation is warranted for greater understanding.

### INFLUENCE OF THE INTERLAYER INTERACTIONS

To assess the dependence of the representative Young's modulus  $E_{\text{rep}}$  on layer charge  $z$ , the surface charge density  $\sigma$  was estimated (Table 2) from the lateral unit-cell dimensions ( $a$  and  $b$ ). A very simple approximation assumes that both the 2:1 layer unit area and associated non-hydrated interlayer cations per unit area act as point charges. The electrostatic force per unit area between the two point charges,  $P$ , is given by

$$P = \frac{1}{4\pi\epsilon_1} \frac{\sigma^2}{r^2} \quad (5)$$

where  $\epsilon_1$  is the electrical permittivity of the phyllosilicates and  $r$  is the distance between the two point charges. Because these 2:1 phyllosilicates have similar crystal structure, density, and chemical composition, it is reasonable to assume that  $\epsilon_1$  is a constant for all samples. Notice that  $P$  is the force per unit area, which is also the average stress. The true Young's modulus  $E$  is then given by

$$E = \frac{ds}{de} = \frac{dP}{dr} = \frac{1}{-2\pi\epsilon_1} \frac{\sigma^2}{r^3} \quad (6)$$

where  $s$  and  $e$  are the stress and strain, respectively. If the center of octahedral sheet is assumed to be the center of the point charge in the  $[001]^*$  direction, owing to the ideal symmetry of the 2:1 layers, then  $r = d(001)/2$ .

Figure 6 shows the relationships between  $E_{\text{rep}}$  and  $[2\sigma/d(001)]^2$ , and between  $E_{\text{rep}}$  and  $\sigma$ . Clearly, a better linear correlation exists for the former than the latter, as reflected by the

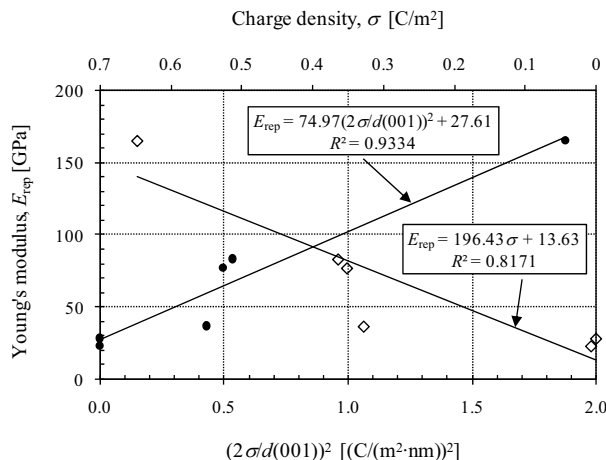


FIGURE 6. Correlations of the representative Young's modulus with  $\sigma$  and  $[2\sigma/d(001)]^2$ .

higher value of the coefficient of determination,  $R^2$ . The non-ideal linear correlations are mainly caused by biotite. As shown in Table 2, when compared with the two muscovite samples, biotite has a slightly smaller charge density, a larger basal spacing, and a different orientation of the O-H vector that weakens the electrostatic attraction between the interlayer cation and the 2:1 layer. Moreover, the chemical composition of biotite may also affect interlayer cohesiveness. An  $\text{Fe}^{2+}$  rich biotite (Table 1) would be expected to behave differently from an Mg-rich biotite or Al-rich muscovite, because of the  $d$  orbitals of iron atoms. In addition, based on the thermal expansion studies of Russell and Guggenheim (1999), the OH vector in an OH-rich mica would be expected to affect the compressibility and stiffness differently compared to a F-rich mica, because the cation-H<sup>+</sup>-oxygen arrangement would tend to repel the interlayer cation if compression forces the cation toward the oxygen, whereas F<sup>-</sup> attracts an interlayer cation. Biotite, including the one studied here, has more F<sup>-</sup> than muscovite (Table 1). Therefore, taking the chemical composition and structure into account, this biotite has a much smaller elastic modulus than either of the two muscovite samples. Nevertheless, the nearly linear correlation (neglecting biotite) shown in Figure 6 suggests that the  $[001]^*$  elasticity of these phyllosilicate minerals with non-hydrated interlayer cations is strongly influenced by the electrostatic attractions between the 2:1 layer and interlayer cations. This is consistent with the conclusion of Zhang et al. (2009a) that different elastic modulus and hardness of muscovite and rectorite are caused by the different interlayer complexes, where rectorite is an expandable, 2:1 phyllosilicate mineral with 50% hydrated and 50% non-hydrated cations and variable basal spacing. The dependence of elasticity of phyllosilicate minerals on the interlayer interactions suggests that the elasticity signatures of these layer silicates originate from the interlayer complexes and how these complexes interact with the layers. Further research is warranted to quantify these elasticity signatures of phyllosilicate minerals for both theoretical understanding and practical applications.

### ACKNOWLEDGMENTS

Financial support from the Louisiana Board of Regents through Contract LEQSF(2007-08)-ENH-TR-24, to assist in the acquisition of a nanomechanical testing and characterization system, is gratefully acknowledged. Z.W. received the Graduate Supplement Award from LSU Graduate School to partially support his graduate study.

### REFERENCES CITED

- Bailey, S.W. (1984) Crystal chemistry of the true micas. In S.W. Bailey, Ed., *Micas*, 13, p. 13–60. Reviews in Mineralogy, Mineralogical Society of America, Chantilly, Virginia.
- Baker, S.P., Vinci, R.P., and Arias, T. (2002) Theme article—elastic and anelastic behavior of materials in small dimensions. *MRS Bulletin*, 27, 26–29.
- Barsoum, M.W., Murugaiah, A., Kalidindi, S.R., and Zhen, T. (2004a) Kinking nonlinear elastic solids, nanoindentations, and geology. *Physical Review Letters*, 92, 255508.
- Barsoum, M.W., Murugaiah, A., Kalidindi, S.R., Zhen, T., and Gogotsi, Y. (2004b) Kink bands, nonlinear elasticity and nanoindentations in graphite. *Carbon*, 42, 1435–1445.
- Chen, B. and Evans, J.R.G. (2006) Elastic moduli of clay platelets. *Scripta Materialia*, 54, 1581–1585.
- Dera, P., Prewitt, C.T., Japel, S., Bish, D.L., and Johnston, C.T. (2003) Pressure-controlled polytypism in hydrous layered minerals. *American Mineralogist*, 88, 1428–1435.
- Doerner, M.F. and Nix, W.D. (1986) A method for interpreting the data from depth-sensing indentation instruments. *Journal of Materials Research*, 1, 601–609.
- Eberhart, M.E. (1996) The metallic bond: elastic properties. *Acta Materialia*, 44, 2495–2504.

- Fischer-Cripps, A.C. (2002) Nanoindentation, 197 p. Springer-Verlag, New York.
- Guggenheim, S. and Bailey, S.W. (1975) Refinement of the margarite structure in subgroup symmetry. *American Mineralogist*, 60, 1023–1029.
- Guggenheim, S., Chang, Y.-H., and Koster van Groos, A.F. (1987) Muscovite dehydroxylation: High-temperature studies. *American Mineralogist*, 27, 537–550.
- Hazen, R.M. and Finger, L.W. (1978) The crystal structures and compressibilities of layer minerals at high pressure. II. Phlogopite and chlorite. *American Mineralogist*, 63, 293–296.
- Johnson, K.L. (1985) Contact mechanics, 452 p. Cambridge University Press, U.K.
- Lee, J.H. and Guggenheim, S. (1981) Single crystal X-ray refinement of pyrophyllite-1T<sub>c</sub>. *American Mineralogist*, 66, 350–357.
- Li, X. and Bhushan, B. (2002) A review of nanoindentation continuous stiffness measurement technique and its applications. *Materials Characterization*, 48, 11–36.
- Manevitch, O.L. and Rutledge, G.C. (2004) Elastic properties of a single lamella of montmorillonite by molecular dynamics simulation. *Journal of Physical Chemistry B*, 108, 1428–1435.
- Mavko, G., Mukerji, T., and Dvorkin, J. (1998) *The Rock Physics Handbook*. Cambridge University Press, New York.
- McNeil, L.E. and Grimsditch, M. (1993) Elastic moduli of muscovite mica. *Journal of Physics: Condensed Matter*, 5, 1681–1690.
- Mencik, J., Munz, D., Quandt, E., Weppelmann, E.R., and Swain, M.V. (1997) Determination of elastic modulus of thin layers using nanoindentation. *Journal of Materials Research*, 12, 2475–2484.
- Molina-Aldareguia, J.M., Emmerlich, J., Palmquist, J.-P., Jansson, U., and Hultman, L. (2003) Kink formation around indents in laminated Ti<sub>3</sub>SiC<sub>2</sub> thin films studied in the nanoscale. *Scripta Materialia* 49, 155–160.
- Oliver, W.C. and Pharr, G.M. (1992) An improved technique for determining hardness and elastic modulus using load and displacement sensing indentation experiments. *Journal of Materials Research*, 7, 1564–1583.
- (2004) Measurement of hardness and elastic modulus by instrumented indentation: Advances in understanding and refinements to methodology. *Journal of Materials Research*, 19, 3–20.
- Oliver, D.J., Bradby, J.E., Williams, J.S., Swain, M.V., and Munroe, P. (2007) Giant pop-ins and amorphization in germanium during indentation. *Journal of Applied Physics* 101, 043524.
- Oliver, D.J., Lawn, B.R., Cool, R.F., Reitsma, M.G., Bradby, J.E., and Williams, J.S. (2008) Giant pop-ins in nanoindented silicon and germanium caused by lateral cracking. *Journal of Materials Research* 23, 297–301.
- Pawley, A.R., Redfern, S.A.T., and Wood, B.J. (1995) Thermal expansivities and compressibilities of hydrous phases in the system MgO-SiO<sub>2</sub>-H<sub>2</sub>O: talc, phase A and 10 Å phase. *Contributions to Mineralogy and Petrology*, 122, 301–307.
- Perdikatsis, B. and Burzlaff, H. (1981) Strukturverfeinerung am talk Mg<sub>3</sub>[(OH)<sub>2</sub>Si<sub>4</sub>O<sub>10</sub>]. *Zeitschrift für Kristallographie*, 156, 177–186.
- Podsiadlo, P., Liu, Z., Paterson, D., Messersmith, P.B., and Kotov, N.A. (2007) Fusion of seashell nacre and marine bioadhesive analogs: high-strength nanocomposite by layer-by-layer assembly of clay and 1-3,4-dihydroxyphenylalanine polymer. *Advanced Materials*, 19, 949–955.
- Rancourt, D.G., Dang, M.Z., and Lalonde, A.E. (1992) Mössbauer spectroscopy of tetrahedral Fe<sup>3+</sup> in trioctahedral micas. *American Mineralogist*, 77, 34–43.
- Russell, R.L. and Guggenheim, S. (1999) Crystal structure of near-end-member phlogopite at high temperatures and heat-treated Fe-rich phlogopite: the influence of the O, OH, F site. *Canadian Mineralogist*, 37, 711–720.
- Schuh, C.A. (2006) Nanoindentation studies of materials. *Materials Today*, 9, 32–40.
- Vaughan, M.T. and Guggenheim, S. (1986) Elasticity of muscovite and its relationship to crystal structure. *Journal of Geophysical Research*, 91, 4657–4664.
- Vernik, L. and Liu, X. (1997) Velocity anisotropy in shales: A petrophysical study. *Geophysics*, 62, 521–532.
- Wang, J., Sinogeikin, S.V., Inoue, T., and Bass, J.D. (2006) Elastic properties of hydrous ringwoodite at high-pressure conditions. *Geophysical Research Letters*, 33, L14308.
- Wang, Z., Wang, H., and Cates, M.E. (2001) Effective elastic properties of solid clays. *Geophysics*, 66, 428–440.
- Zanazzi, P.F., Montagnoli, M., Nazzareni, S., and Comodi, P. (2007) Structural effects of pressure on monoclinic chlorite: A single-crystal study. *American Mineralogist*, 92, 655–661.
- Zhang, G., Wei, Z., and Ferrell, R.E. (2009a) Elastic modulus and hardness of muscovite and rectorite determined by nanoindentation. *Applied Clay Science*, 43, 271–281.
- (2009b) Reply to comment on “Elastic modulus and hardness of muscovite and rectorite determined by nanoindentation.” *Applied Clay Science*, 46, 429–432.

MANUSCRIPT RECEIVED SEPTEMBER 5, 2009

MANUSCRIPT ACCEPTED JANUARY 29, 2010

MANUSCRIPT HANDLED BY LARS EHM